Astronomy & Astrophysics manuscript no. HD142527_V8.1_arxiv
December 20, 2018

SPHERE dynamical and spectroscopic characterization of HD142527B ⋆

R. Claudi[1], A.–L. Maire[2], D. Mesa[1,3], A. Cheetham[4], C. Fontanive[5], R. Gratton[1], A. Zurlo[6,7,8], H. Avenhaus[9,10,11], T. Bhowmik[12], B. Biller[2,5], A. Boccaletti[12], M. Bonavita[1,5], M. Bonnefoy[13], E. Cascone[14], G. Chauvin[13,15], A. Delboulbé[13], S. Desidera[1], V. D'Orazi[1], P. Feautrier[13], M. Feldt[2], F. Flammini Dotti[1,27], J.H. Girard[13,16], E. Giro[1], M. Janson[2,18], J. Hagelberg[13], M. Keppler[2], T. Kopytova[2,19], S. Lacour[12], A.–M. Lagrange[13], M. Langlois[8,20], J. Lannier[13], H. Le Coroller[8], F. Menard[13], S. Messina[21], M. Meyer[9,23], M. Millward[22], J. Olofsson[2,24,25], A. Pavlov[2], S. Peretti[4], C. Perrot[12], C. Pinte[13,26], J. Pragt[28], J. Ramos[2], S. Rochat[13], L. Rodet[13], R. Roelfsema[28], D. Rouan[12], G. Salter[8], T. Schmidt[12], E. Sissa[1], P. Thebault[12], S. Udry[4], A. Vigan[8].

(Affiliations can be found after the references)

Received ....; accepted .....

ABSTRACT

Aims. HD142527 is one of the most frequently studied Herbig Ae/Be stars with a transitional disk that hosts a large cavity that is up to about 100 au in radius. For this reason, it has been included in the guaranteed time observation (GTO) SpHere INfrared survey for Exoplanets (SHINE) as part of the Spectro-Polarimetric High-contrast Exoplanet REsearch (SPHERE) at the Very Large Telescope (VLT) in order to search for low-mass companions that might explain the presence of the gap. SHINE is a large survey within about 600 young nearby stars are observed with SPHERE with the aim to constrain the occurrence and orbital properties of the giant planet population at large (> 5 au) orbital separation around young stars.

Methods. We used the IRDIFS observing mode of SPHERE (IRDIS short for infrared dual imaging and spectrograph plus IFS or integral field spectrograph) without any coronagraph in order to search for and characterize companions as close as 30 mas of the star. Furthermore, we present the first observations that ever used the sparse aperture mask (SAM) for SPHERE both in IRDIFS and IRDIFS_EXT modes. All the data were reduced using the dedicated SPHERE pipeline and dedicated algorithms that make use of the principal component analysis (PCA) and reference differential imaging (RDI) techniques.

Results. We detect the accreting low–mass companion HD142527B at a separation of 73 mas (11.4 au) from the star. No other companions with mass greater than 10 M_J are visible in the field of view of IFS (∼ 100 au centered on the star) or in the IRDIS field of view (∼ 400 au centered on the star). Measurements from IFS, SAM IFS, and IRDIS suggest an M6 spectral type for HD142527B, with an uncertainty of one spectral subtype, compatible with an object of M= 0.11 ± 0.06 $M_\odot$ and R= 0.15 ± 0.07 $R_\odot$. The determination of the mass remains a challenge using contemporary evolutionary models, as they do not account for the energy input due to accretion from infalling material. We consider that the spectral type of the secondary may also be earlier than the type we derived from IFS spectra. From dynamical considerations, we further constrain the mass to $0.26^{+0.16}_{-0.14}$ $M_\odot$, which is consistent with both our spectroscopic analysis and the values reported in the literature. Following previous methods, the lower and upper dynamical mass values correspond to a spectral type between M2.5 and M5.5 for the companion. By fitting the astrometric points, we find the following orbital parameters: a period of P= 35 − 137 yr; an inclination of i = 121 − 130° , a value of Ω = 124 − 135° for the longitude of node, and an 68% confidence interval of ∼ 18 − 57 au for the separation at periapsis. Eccentricity and time at periapsis passage exhibit two groups of values: ∼0.2–0.45 and ∼0.45–0.7 for e, and ∼2015–2020 and ∼2020–2022 for T_0. While these orbital parameters might at first suggest that HD142527B is not the companion responsible for the outer disk truncation, a previous hydrodynamical analysis of this system showed that they are compatible with a companion that is able to produce the large cavity and other observed features.

Key words. Star: Formation, Protoplanetary Disks, Instrumentation: high angular resolution, Techniques: imaging spectroscopy, Stars: Individual: HD142527

1. Introduction

Planet formation from disks (Williams & Cieza 2011; Mordasini et al. 2015) imprints characteristic structures on the disks (e.g., Muto et al. 2012). One of the most striking structures that can be produced in this manner are the wide gaps carved by massive or multiple forming planets in protoplanetary disks (Dodson-Robinson & Salyk 2011; Zhu et al. 2011). Disks with large gaps, or cavities, are often referred to as "transitional disks", and they are observed around Herbig stars or their less massive counterparts, TTauri stars (Strom et al. 1989). A striking example of a transitional disk is the young Herbig Ae star (F6III, age∼ 5 Myr) HD142527 (Fukagawa et al. 2006) with its large gap. HD142527 shows a cavity as large as ∼ 100 au in radius. For this reason, it is one of the most freequently studied objects of this type (see Section 2). Transitional disks are believed to be in the evolutionary stage between optically thick gas-rich disks and older disks where most of the gas has been dissipated (see, e.g., Espaillat et al. (2014) and references therein). In a handful of cases the

⋆ Based on observations collected at the European Organisation for astronomical research in the southern emisphere under ESO programmes 095.C–0298, 096.C–0241, 097.C–0865 and 189.C–0209.

connection between the presence of a gap and the existence of (candidate) low-mass companions has been established. Some companion candidates were discovered in the LkCa 15 system (Kraus & Ireland 2012; Sallum et al. 2015), MWC 758 (Reggiani et al. 2017), HD169142 (Reggiani et al. 2014; Biller et al. 2014; Osorio et al. 2014; Fedele et al. 2017; Ligi et al. 2018), and HD100546 (Mulders et al. 2013; Quanz et al. 2013, 2015; Brittain et al. 2013, 2014; Quanz et al. 2015). HD142527 also has a low-mass companion that resembles an M star (Lacour et al. 2016). The recent advent of dedicated high-contrast imagers such as Spectro-Polarimetric High-contrast Exoplanet REsearch (SPHERE, Beuzit et al. 2008), Gemini Planet Imager (GPI, Macintosh et al. 2014), and Subaru Coronagraphic Extreme Adaptive Optics (SCExAO, Jovanovic et al. 2016) offers the possibility to probe regions of transitional disk systems that lie closer to the star than was possible with previous imaging instruments and to constrain the presence of any companion that could be responsible for opening up an observed gap or cavity.

In this paper we present new deep images of the central regions of the HD142527 system obtained with SPHERE as part of the SPHERE consortium guaranteed time observations (GTO). These data include both non-coronagraphic direct images and sparse aperture masking (SAM) data acquired with the near-infrared channels integral field spectrograph (IFS) and infra-red dual imaging and spectrograph (IRDIS). The outline of the paper is as follows: in Sect. 2 we summarize the main characteristics of the HD142527 system. In Sect. 3 we describe the SPHERE near-infrared observations; in Sect. 4 we describe the reduction methods we applied, and the results are discussed in Sect. 5. The mass estimate of the companion is discussed in Sect. 6, and the orbital properties of HD142527B are derived in Sect. 7. In Sect. 8 we outline the conclusions.

2. HD142527

HD142527 is a young 5 ± 1.5 Myr (Mendigutía et al. 2014) intermediate-mass star at a distance of 140 ± 20 pc from the Sun (Acke & van den Ancker 2004; Mendigutía et al. 2014). Its spectral type of F6 IIIe (Houk 1978; Henize 1976; Waelkens et al. 1996) corresponds to a mass of 2.0 ± 0.3 $M_\odot$, (Fukagawa et al. 2006; Verhoeff et al. 2011). We adopt the distance recently refined by Gaia Collaboration et al. (2016) to 156^{+7}_{-6} pc and the proper motion of $\mu_\alpha = -11.76 \pm 0.08$ mas/yr, $\mu_\delta = -24.45 \pm 0.05$ mas/yr.

HD142527 is one of the most frequently studied Herbig Ae/Be stars with a transitional disk because its disk is seen almost face-on and its protoplanetary cavity, extending to a radius of about 100 au, can be investigated because of its record size (Fukagawa et al. 2006). The gap in this system extends to between 30 and 130 au (Verhoeff et al. 2011), and the outer disk extends to about 600 au. The system is seen at a low inclination: $i = 28 \pm 3°$ (Perez et al. 2015). The HD142527 disk has long been posited as a possible site of planet formation because of the extremely high fraction of crystalline silicates, which have possibly formed by a massive companion that induced spiral density waves in the disk material (van Boekel et al. 2004; Avenhaus et al. 2017). Fukagawa et al. (2006) imaged in scattered light the outer edge of the gap as well as a spiral feature in the outer disk. These features have recently been confirmed in the visible polarized light by Avenhaus et al. (2017). The protoplanetary disk of HD142527 shows high near-infrared excess (Malfait et al. 1999; Fukagawa et al. 2006) that indicates that optically thick material lies close to the star; this might be a remnant of the original inner disk. The central star still accretes at a rate of 9.5×10^{-8} $M_\odot$/yr (Garcia Lopez et al. 2006; Casassus et al. 2012; Avenhaus et al. 2014; Biller et al. 2012; Salyk et al. 2013), suggesting that there is still enough material close to the star for it to be funneled onto the star. The outer radius of this inner disk is likely within 10 au (Verhoeff et al. 2011; Fukagawa et al. 2013; Close et al. 2014). Fukagawa et al. (2006) also found an offset of 20 au between the location of the star and the center of the disk, which may be caused by an unseen (at the epoch) eccentric binary companion. The gap appears to be completely depleted of both large and small dust grains, as evidenced from scattered light images as well as (sub-) millimeter observations. Nonetheless, CO gas has been detected within the gap (Casassus et al. 2013).

Using SAM with NACO (short for NAOS-CONICA or Nasmyth adaptive optics system near infrared imager and spectrograph, Tuthill et al. 2010) at the Very Large Telescope (VLT), Biller et al. (2012) detected an asymmetry in the brightness distribution around the central star with a barycenter emission located at a projected separation of 88 ± 5 mas (12.8 ± 1.5 au at 145 pc) and flux ratios in H,K, and L' of 0.016 ± 0.007, 0.012 ± 0.008, and 0.0086 ± 0.0011, respectively (3σ errors), relative to the primary star and disk. They interpreted this asymmetry as a low-mass stellar companion ($\sim$ 0.2 $M_\odot$) orbiting at $\approx$ 12 au from the star, well inside the gap. On the basis of their observations with near infrared coronagraphic imager (NICI) at Gemini south, Casassus et al. (2013) disputed the presence of a companion, but Close et al. (2014) confirmed the companion's existence through direct-imaging observations in the R and in H_α bands. The latter implies mass accretion, and the authors quantified it as $\sim 5.9 \times 10^{-10}$ $M_\odot$ yr^{-1}. Recently, Lacour et al. (2016) observed HD142527 from *R*− to *M*–band wavelengths with the NACO and Gemini Planet Imager (Greenbaum et al. 2014) instruments using the SAM technique. They constrained the companion mass and radius with evolutionary models as 0.13 ± 0.03 $M_\odot$ and 0.90 ± 0.15 $R_\odot$, respectively, and derived a younger age ($1.0^{+1.0}_{-0.75}$ Myr) than for HD142527A. The characteristics of this system, and in particular the existence of the wide gap beyond the low-mass companion, make the HD142527 system a prime target for the search for circumbinary planets (Bonavita et al. 2016).

3. Observations

The SPHERE planet-finder instrument installed at the VLT (Beuzit et al. 2008) is a highly specialized instrument dedicated to high-contrast imaging at optical and near-infrared wavelengths. It is equipped with an extreme adaptive optics system called SAXO (Sphere Adaptive Optics for eXoplanet Observation) (Fusco et al. 2014; Petit et al. 2014), with a 41 × 41 actuator wavefront control, pupil stabilization, and differential tip-tilt control. It also employs stress-polished toric mirrors for beam transportation (Hugot et al. 2012). The SPHERE instrument is equipped with several coronagraphic devices for stellar diffraction suppression, including apodized Lyot coronagraphs (Soummer 2005) and achromatic four-quadrant phase masks (Boccaletti et al. 2008). The instrument has three science subsystems: the infrared dual-band imager and spectrograph (IRDIS; Dohlen et al. 2008), an integral field spectrograph (IFS; Claudi et al. 2008, 2016), and a rapid-switching imaging polarimeter (ZIMPOL; Thalmann et al. 2008).

Our observations were part of the SHINE (SpHere INfrared survey for Exoplanets, Chauvin et al. 2017) survey and were performed with SPHERE in the IRDIFS_EXT mode (direct imaging). In this mode, IRDIS observes in dual-band imaging (DBI; Vigan et al. 2010) with the K12 filter pair (wavelength K1=2.110

Table 1. HD142527 Observations.

UT Date	Instr. Mode	Instr.	Filter	DIT×NDIT[a] (s)	N^a_{exp}	Field Rot. (°)	Seeing (")	Strehl @1.6μm	True North Correction (°)
2015-05-13	IRDIFS_EXT	IFS	YJH/ND1	4.0 ×56	8	40.10	0.3	0.8	−1.86 ± 0.15
		IRDIS	K1–K2/ND1	0.84 ×88	16				
		IFS	YJH/ND2	8.0 ×8	8				
		IRDIS	K1–K2/ND2	8.0 ×8	8				
2015-07-03	SAM	IFS	YJ	4 × 8	3	25.00	0.5	0.7	−1.768 ± 0.055
		IRDIS	H2–H3	0.84 ×32	12				
2016-03-26	IRDIFS_EXT	IFS	YJH/ND1	4.0 ×56	16	73.84	0.7	0.7	−1.756 ± 0.061
		IRDIS	K1–K2/ND1	0.84 ×88	32				
		IFS	YJH/ND2	8.0 ×8	12				
		IRDIS	K1–K2/ND2	2.0×19	12				
2016-06-13	IRDIFS_EXT	IFS	YJH/ND1	4.0×60	16	64.48	0.8	0.6	−1.664 ± 0.048
		IRDIS	K1–K2/ND1	0.84 ×49	64				
2017-05-16	SAM	IFS	YJH	4.0×16	24	73.00	0.6	0.7	−1.800 ± 0.052
		IRDIS	K1–K2	0.84 ×32	4				
		IRDIS	K1–K2	0.84 ×52	20				
2018-04-14	SAM	IFS	YJH	2.0×18	16	52.00	0.6	0.9	−1.75 ± 0.10
		IRDIS	K1–K2	0.84 ×36	16				

[a] NDIT refers to the number of integrations per datacube, DIT to the integration time, N_{exp} to the number of datacubes

μm; K2=2.251 μm), while IFS obtains low-resolution (R=30) spectra between 0.95 and 1.65 μm. The target has been observed with SAM both in IRDIFS and IRDIFS_EXT mode. In contrast to the IRDIFS_EXT mode, in the IFS mode IRDIS observes in dual-band imaging with H23 filter pair (wavelength H2=1.589 μm; H3=1.667 μm), while IFS performs low-resolution spectroscopy at R$\sim$ 50 in the wavelength range 0.95 – 1.35 μm.

3.1. Direct imaging

We observed HD142527 during five nights (2015–03–13, 2016–03–26, 2016–06–13, 2017–05–16, and 2018–04–14) as part of the SPHERE GTO program (IRDIFS and SAM) plus one in technical time dedicated to the commissioning of the SAM observing mode (2015–07–03). The instrumental setups used during these observations are all described in Table 1. The main goal of these observations was to detect and characterize the stellar companion around HD142527 and to place strong constraints on the presence of other possible companions. Because the star – companion separation is expected to be smaller than (88 ± 5 mas), we observed the star without a coronagraph, and adjusted the exposure time in order to avoid detector saturation. In the first two observations with the modified IRDIFS_EXT instrument mode (no coronagraph), the IRDIS images taken with the 1/10 neutral density filter (ND1) were slightly saturated. For this reason we took additional unsaturated exposures using the 1/100 neutral density (ND2) filter to properly calibrate the flux from the star and ND1 images. No saturation was present in the IFS images, so all IFS images could be used as science images. The observing conditions were worse for the IRDIS observations, which are not saturated on the third night, so that we were able to use only the ND1 filter to take our science images. In order to attenuate the residual speckle noise with the angular differential imaging (ADI; Marois et al. 2006a) technique in the post-processing phase, we acquired our observations in pupil-stabilized mode.

3.2. Sparse aperture masking

HD142527 was also observed in the SAM mode of SPHERE (Cheetham et al. 2016) on the night of March 7, 2015, during a technical night to test this observing mode, and additionally, as part of SHINE, on the nights of May 16, 2017, and April 14, 2018. This was the first time in which the SAM mode was used with SPHERE. The object was observed in IRDIFS (July 3, 2015) and in IRDIFS_EXT (May 16, 2017 and April 14, 2018) modes with a seven-hole pupil-aperture mask with the same layout as was used with NACO. The observing conditions during the 2015 observation were poor, with thick clouds, low-coherence times, and high values of seeing affecting the performance of the AO system.

To calibrate the systematic effects that are present in SAM (and similar interferometric techniques), the calibrator stars HD 142695 and HD 142277 were also observed. The observations used 0.84 s and 8 s exposure times for IRDIS and IFS, respectively (see Table 1).

4. Data reduction and analysis

The data gathered in the six observation nights have been reduced following the necessary data reduction recipes for the individual instruments in both the classical (IRDIFS) mode and IFS and IRDIS in SAM mode. In this paragraph the data reduction is discussed for each instrument.

4.1. IFS data

For the IFS data we began with the reduction of calibration data (dark, detector flat, spectral position frames, wavelength calibration, and instrument flat) using the data reduction and handling (DRH) software (Pavlov et al. 2008). For a more detailed description of each of these steps, we refer to Mesa et al. (2015). The raw science data frames were then averaged so that the rotation between any two frames was on the order of 0.3 degrees. This left us with 128 different frames for the first night and 248

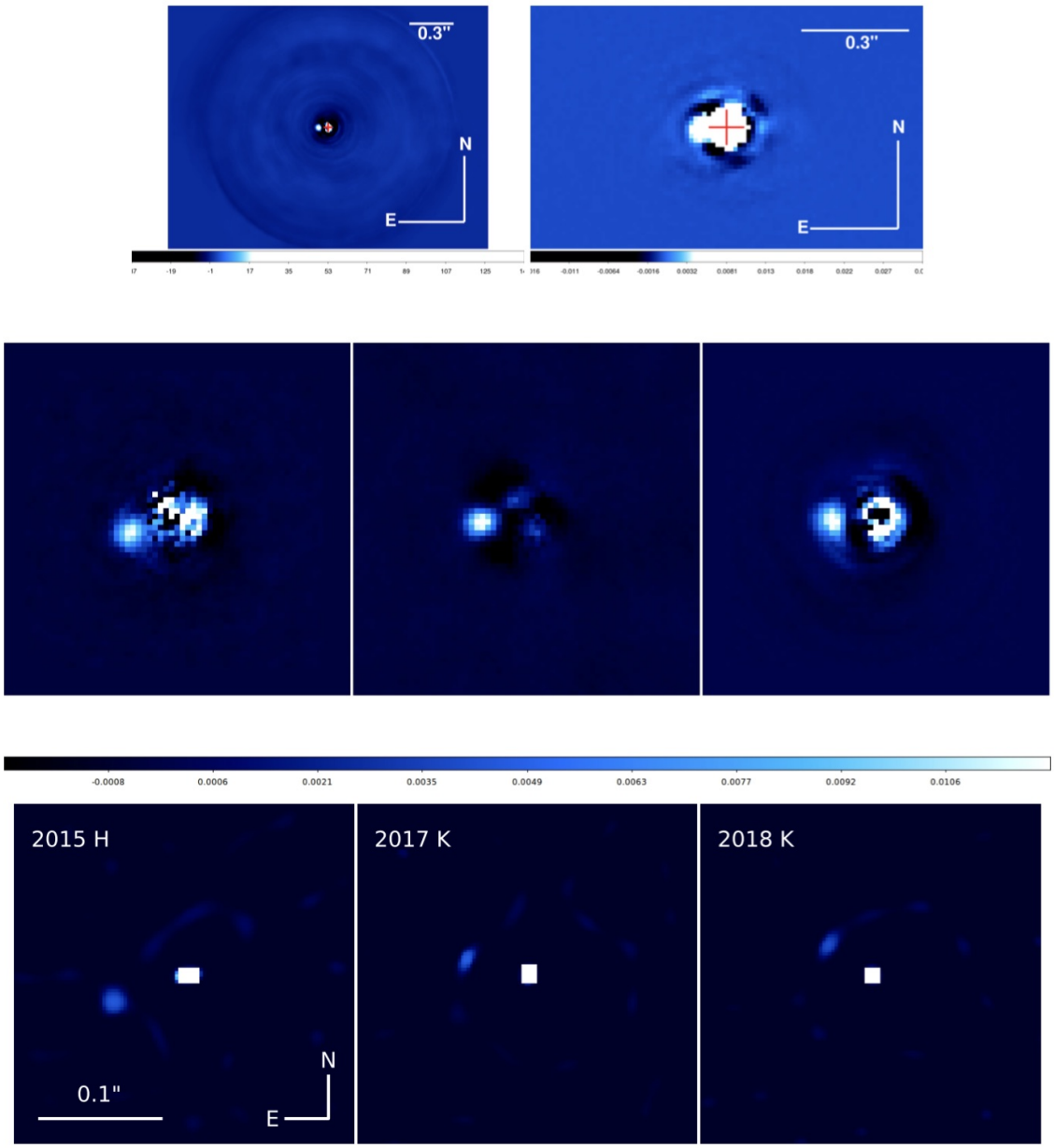

Fig. 1. Non-coronagraphic IRDIFS_EXT and SAM images of the HD142527 system. **Upper panel**: Images acquired on June 13, 2016. **Left**: PCA post-processing IFS image (averaged over all channels). The red cross marks the position of the central star. In this image the companion of HD142527 is clearly visible. **Right**: Central part of the PCA post-processing IRDIS image of HD142527. **Central panel**: Composition of the three RDI post-processing IFS images (from left to right: May 2015, March 2016, and June 2016). The orbital motion of B is clearly detected. **Bottom panel**: Reconstructed images produced from the SAM data using the MiRA algorithm. The images show that we observe significant orbital motion for the companion HD 142527B between the SAM epochs, and that the point-source model used to calculate its position is a good approximation to the observed structure

for the second night, when a larger dataset was obtained. For the third night, we had 96 frames after binning. For each of these frames, we then corrected the bad pixels and the effects of the cross-talk between different lenslets of the IFU (Antichi et al. 2009) using dedicated IDL procedures described in more detail in Mesa et al. (2015). On each frame, we then ran the DRH science recipe, which uses the calibration files and produces a wavelength-calibrated datacube composed of 39 monochromatic images. Each of these images was then corrected for the different exposure times and neutral density filters used. We then determined the position of the star for each frame using the CNTRD[1] IDL procedure and recentered each of them to the nominal position of the image center. Finally, to retrieve the companion image, we performed a principal component analysis (PCA) procedure as described in Mesa et al. (2015), exploiting both the angular and spectral information. As we observed the object in a non-coronagraphic mode and to reduce concern for the self-cancellation that is present in the PCA method, we also performed a point spread function (PSF) subtraction (reference differential imaging, RDI) in a region very close to the star. We devised an automatic search in the SPHERE Data Cen-

[1] http://www.harrisgeospatial.com/docs/cntrd.html

ter (SDC, Delorme et al. 2017) for reference sequences obtained using the same observing mode (non-coronagraphic observation in IRDIFS_EXT mode). We found that the best match was an observation of HD100546, which provides the highest correlation with the observation of HD142527, taken in February 2017, although this star also hosts a bright disk. This sequence includes 533 individual 3D (x, y, lambda) datacubes. We are aware that HD100546 has a bright disk that is well visible in scattered light (see, e.g., Sissa et al. (2018)). However, first, the model is obtained by an automatic procedure. Second, the inner disk of HD 100546 is not resolved in SPHERE images and the apparent separation of the inner edge of the intermediate ring is at about twice that of the companion of HD142527. Hence, the disk of HD 100546 has no impact on the present discussion. For each separate wavelength image, we first accurately recentered each image on the peak of the diffraction image. For each monochromatic image of the science datacube, our code then searched for the monochromatic image of the reference datacube that provides the highest cross-correlation within a circle with a radius of 12 pixels from the nominal center. This is selected as the best -matching monochromatic image. The flux of the best-matching monochromatic image is normalized to the value of the science monochromatic image and then subtracted. The subtracted image is normalized to the peak of the original image, thus we therefore obtain a contrast image. The subtracted monochromatic image is derotated and a median of the derotated monochromatic images is then made over time. A high-pass filtering is then made by subtracting the current median over an area of 21×21 pixels centered on each pixel. The final images are then obtained by collapsing the datacubes along the spectral axis.

4.2. IRDIS data

Data reduction for the IRDIS observations was performed following the procedures described in Zurlo et al. (2014, 2016). The IRDIS raw images were pre-reduced by performing background subtraction, bad-pixel correction, and flat fielding. As these are non-coronagraphic images, no satellite spots or PSF reference images were taken. Satellite spots are fiducial spots symmetric with respect to the central star created by using a periodic grid mask downstream a coronagraph (Sivaramakrishnan & Oppenheimer 2006; Marois et al. 2006b) or by applying a periodic modulation on an adaptive optics deformable mirror (Langlois et al. 2013). We used one of the images in the sequence as a reference in order to apply the SDC data reduction procedure. The frames within the resulting datacube were then aligned with one another after finding for each of them the location of the star using the CNTRD IDL procedure and recentering each of them to the nominal position of the image center. For all epochs, after the preprocessing of each frame, the speckle pattern subtraction was performed using both the PCA (Soummer et al. 2012) and the TLOCI (Marois et al. 2014) algorithms, combined with the ADI technique.

4.3. Sparse aperture masking data analysis

The SAM IFS data were converted into cleaned wavelength-extracted cubes using the SPHERE DRH in the same manner as the coronagraphic frames, but without any data binning. The IRDIS and IFS wavelength cubes were then processed using the IDL-based aperture masking pipeline developed at the University of Sydney, with recent modifications allowing the simultaneous processing of multiwavelength data. A more thorough description of the pipeline can be found in Tuthill et al. (2000), Kraus et al. (2008), and the references therein, but a brief summary follows.

The data were background subtracted, flat fielded, and cleaned of bad pixels and cosmic rays. The cleaned cubes were then windowed with a super-Gaussian function of the form $e^{(-ar^4)}$ before closure phases were extracted from the Fourier transforms of the images. Calibration of the closure phases was performed on each wavelength individually by subtracting a weighted sum of the corresponding measurements taken on the calibrator stars.

The calibrated closure phases were fit with a binary analytical model with the following free parameters: the separation, position angle, and a contrast value for each wavelength channel. The IFS and IRDIS data were fit separately, resulting in four free parameters for IRDIS and 41 parameters for IFS. The best-fit parameters were estimated using *emcee* - a Python implementation of the affine-invariant Markov chain Monte Carlo (MCMC) ensemble sampler (Foreman-Mackey et al. 2013). To account for uncalibrated systematics, a constant was added in quadrature to each closure phase uncertainty to ensure that the best-fitting model had a reduced χ^2 of 1. These constants were estimated to be 0.45° and 0.4° for IRDIS and IFS, respectively, in comparison to initial median uncertainties of 0.3° and 0.4°. These high values suggest that the imperfect calibration dominates the uncertainties.

To estimate the detection limits from the observations, a Monte Carlo simulation was performed. We generated a set of 10,000 simulated datasets drawn from a Gaussian distribution, consistent with the measured uncertainties. For each point on a grid of separation and contrast, our detection limits were defined as the point at which at least 99.9% of the datasets were fit better by a point-source model than the binary model. The 99.9% criteria yields a set of 3.3σ detection limits, which were approximately 7.5 mag for separations between 50-250 mas.

5. Results

The final non-coronagraphic images for IFS, IRDIS, and SAM are shown in Figure 1. Images are from the last night of IRDIFS_EXT observations; similar images were obtained on the other two nights when the system was observed with the same instrumental mode. The companion is clearly visible in the IFS images with a signal-to-noise ratio (S/N) of ∼30 (the procedure used to evaluate the S/N is fully described in Zurlo et al. 2014), but it is only marginally resolved in the IRDIS frames because of the very small angular separation of the companion and the less favorable pixel scale of IRDIS. Therefore, we did not use the IRDIS non-coronagraphic data for the astrometric and photometric characterization of HD142527B. The central panel of the same figure shows a composition of three post-processing IFS images of the HD142527 system taken at different epochs (May 2015, March 2016, and June 2016). The companion is also clearly visible in the SAM data with an S/N greater than 60 with IRDIS and greater than 40 with IFS. The S/N in the SAM observations was calculated by comparison of the best-fit flux ratio with the detection limits.We used the MiRA image reconstruction algorithm (Thiébaut 2008) to produce the images in the bottom panel of Figure 1. MiRA uses an inverse-problem approach to reconstruct an image from the limited information provided by the closure phases and power spectrum. The images confirm that the data are consistent with a binary companion and show its orbital motion between the IFS and SAM datasets.

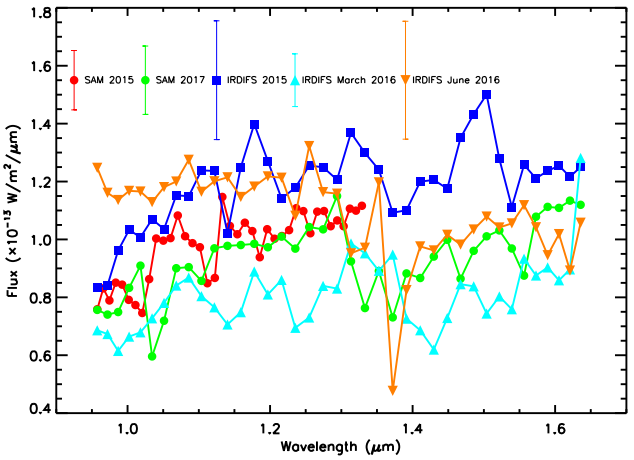

Fig. 2. Comparison among the extracted spectra for HD142527B obtained by both direct imaging and SAM modes of SPHERE in the IFS wavelength range (0.95 – 1.65 μm). In the upper part of the plot is indicated the value of the average value of the error for each spectrum. The SAM IFS spectrum taken in 2015 is limited to the YJ band of IFS (0.95 – 1.35 μm). For a clearer view of the plot all points are connected by continuous lines.

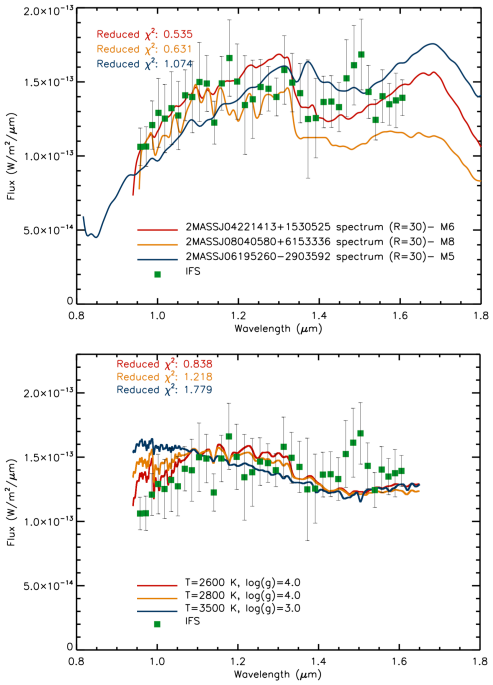

Fig. 3. Top: Extracted spectrum for HD142527B (green squares) compared with the three best-fit spectra (red, orange, and blue solid lines) from the Allers & Liu (2013) obtained from the data taken on the night of May 13, 2015. **Bottom**: Same as the left panel, but compared with the three best-fit models (red, orange, and blue solid lines) from the BT-Settl library Allard (2014).

5.1. HD142527B spectrum

Figure 1 shows that the PCA and RDI post-processing techniques allow us to very clearly detect HD142527B in IFS data. However, at this small separation, self-subtraction will severely diminish the flux in the spectrum of the companion. To avoid self-subtraction due to PCA, we calculated photometry from each IFS spectral channel and the corresponding errors from images obtained with RDI, exploiting the method described in Zurlo et al. (2014). All the extracted spectra (for IFS and SAM) are shown together in Figure 2. In order to facilitate comparison between the spectra taken at different epochs, we plot only points falling in the IFS wavelength range (0.95 – 1.65 μm). The H_2 H_3 and K_1 K_2 points from SAM observations are not shown, but are listed in Table 2.

Each extracted spectrum of HD142527B can be fit with spectra of young field dwarfs from Allers & Liu (2013) to estimate its spectral type. This procedure was executed for all the epochs, and the results are shown in Table 3. The low reduced χ^2 values (< 1) that we obtain in some fits are probably due to the combination of two effects: *i*) all the errors could be overestimates, and *ii*) some of the 39 measurements of each spectrum could have a certain covariance degree between closer spectral channels. The fit is useful, however, to form an impression of the spectral type of the secondary. Figure 3 shows the best-fitting spectra overlaid on the IFS spectrum from May 14, 2015. In order to constrain the physical characteristics of the companion, we compared the extracted spectra with a set of BT-Settl models (Allard 2014). The models were selected in a grid with the effective temperature and the surface gravity ranging in the following intervals: $1000 \leq T_{eff} \leq 4000$ K and $3.0 \leq \log(g) \leq 5.5$, with an incremental step of 100 K for the former and 0.5 for the latter. In all cases the fit with models with $T_{eff} = 2600 - 2800$ K and $\log(g) \sim 4.0$ was good, also when higher temperatures and lower surface gravities were included. As an example of the obtained results, we show in the right panel of Figure 3 the models and in the left panel, we show the same, but fit with the best-fit spectra.

The fit results for a range of spectral types are presented in Table 3. The best-fit spectra match well at all epochs (except for the spectrum from June 13, 2016), thus we determine a spectral type between M5 and M6 for HD142527B with an uncertainty of ±1 subtype, in agreement with the model fitting. From Pecaut & Mamajek (2013) we obtained the value of the T_{eff} corresponding to the best-fit spectral type for each individual observation (Col. 3 of Table 3). The extracted spectra seem to be different from each other (see Figure 2). We evaluated the Y–H color of each spectrum using the value of the magnitude discussed in the next section and reported in Table 2. We obtain a variation from 0.85 up to 1.40 with an average value of 1.16 ± 0.20 for the Y–H color. Even if the Y–H color of HD142527B seems to change at different epochs, the measurement errors we estimate therefore do not allow us to be confident about this color variation. This is also supported by the spectrum obtained in the night of June 13, 2016, which has a bluer color (Y–H= 0.85 ± 0.28) than the others, but has a later spectral type (M7V, see Table 3) according to the fitting procedure with young field dwarf spectra. These results do not allow us to draw a firm conclusion on the spectral type of HD142527B. It could be both later or earlier than the M5–M6 spectral type stated here.

5.2. Photometry

We estimated the wide-band photometry in the Y, J, and H spectral bands by adopting a distance of 156 pc and using the magnitude for the star obtained from 2MASS (Cutri et al. 2003). We combined the median contrasts obtained for all the wavelength channels below 1.15 μm for the Y band, between 1.15 and 1.35 μm for the J band, and between 1.35 and 1.65 μm for the H band.

Table 2. Absolute magnitudes of HD142527 B obtained from the IFS data for Y, J, and H spectral bands. SAM data also contain the H_2, H_3 and K_1 and K_2 bands of IRDIS . These magnitudes are not corrected for the several reddening contributions from the inner part of the HD142527 system (see text).

Date	Y	J	H	H_2	H_3	K_1	K_2
2015-05-13	5.19±0.22	4.91±0.16	4.01±0.17				
2015-07-03	5.38±0.12	5.09±0.09		3.98±0.03	3.93±0.03		
2016-03-26	5.59±0.11	5.33 ±0.09	4.44±0.12				
2016-06-13	5.07±0.22	4.99±0.18	4.22±0.17				
2017-05-16	5.47±0.13	5.20±0.14	4.27±0.10			3.72±0.01	3.71±0.02
2018-04-14						3.69±0.03	3.74±0.04

We derived median contrasts for the H2 and H3 bands from the July 2015 non-coronagraphic SAM image, and median contrasts for the K1 and K2 bands were derived from the May 2017 and April 2018 dataset. The uncertainty on the contrast was then calculated from the median on the error on each single channel in the wavelength ranges defined above. These values were then transformed into the absolute magnitude for HD142527B and are listed Table 2, where the error bars are calculated taking into account the uncertainties on the distance of the system reported in Section 1. From the values listed in Table 2, we obtain Y= 5.34±0.21 mag, J= 5.10±0.17 mag, and H= 4.23±0.19 mag as mean values for the absolute magnitudes of the secondary.

In the determination of the absolute magnitudes of HD142527B, we considered that the interstellar reddening correction for the primary and the secondary are identical, that is, assuming for the system a visible extinction of $A_V = 0.6$ (Verhoeff et al. 2011; Lacour et al. 2016) and a dust reddening of $R_V = 3.1$ as obtained by Weingartner & Draine (2001), we obtain a value of $E(B-V) = 0.194$. From the analysis of the SED of HD142527B, Lacour et al. (2016) stated that the emission in J or bluer bands are almost exclusively (> 90 %) due to the stellar surface. The remaining 10%, which is due to the circumstellar emission, mainly affects the J band, but the Y band is assumed to be unaffected. However, the red color of HD142527B (J-H= 0.87 ± 0.25 mag) is consistent with the presence of an optically thick circum-secondary disk around HD142527B itself, as has previously been identified by Lacour et al. (2016) and Biller et al. (2012). Furthermore, Close et al. (2014), were able to detect HD142527B by means of H_α (0.656 μm) observations that also allowed them to evaluate the mass accretion rate onto HD142527B (5.9×10^{-10} $M_\odot$ yr^{-1}), which is about 1% of the accretion onto the primary star (Close et al. 2014). Both these contributions (the disk and the accretion) are significant at longer wavelengths. From the NIR photometry of Biller et al. (2012), we can assume, as Close et al. did, a ∼ 0.3 mag disk H excess. To correct the absolute magnitudes for these contributions, we used the Cardelli et al. (1989) algorithm and obtained a J-band correction of 0.1 mag and $0.3A_H = 0.09$ mag for the H band. To summarize, the absolute magnitudes of HD142527B, taking into account the circumsecondary material discussed before, become Y= 5.34 ± 0.21 mag, J_{coor} = 5.20 ± 0.17 mag and H_{corr} = 4.31 ± 0.19 mag.

It is worth pointing out that the ZIMPOL polarimetric observation made by Avenhaus et al. (2017) did not find any flux enhancement that would have been due to a dust disk around HD142527B, even though they reached a better contrast than the observations reported in Rodigas et al. (2014), where such a disk is observed. Therefore Avenhause et al. did not confirm the presence of the circum-secondary disk. However, considering a simple model of a reflective optical disk with a radius ≤ 1/3 R_{hill} around the secondary, hence at about 13 au (80 mas at 156 pc) from the primary, it is possible to estimate that the contrast between the primary and the disk is about 11 mag. This contrast value is below the 3σ limit for the observation of HD142527 presented by Avenhaus et al. (2017, panel a of their Figure 2).

Table 3. Reduced χ^2 value for the fits of the HD142527B with the cool field dwarfs of the Allers & Liu (2013) sample. The effective temperatures of the different spectral types are taken from Pecaut & Mamajek (2013).

Date	Sp	T_{eff}	Reduced χ^2
2015-05-13	M6V[a]	2850 ± 200	0.443
2015-07-03	M5V[b]	3030 ± 200	1.013
2016-03-26	M5V[b]	3030 ± 200	1.760
2016-06-13	M7V[c]	2650 ± 200	0.419
2017-05-16	M6V[a]	2850 ± 200	1.035

[a] 2MASSJ04221413+1530525
[b] 2MASSJ06195260–2903592
[c] 2MASSJ05575096–1359503

These magnitudes suggest some degree of variability between the different epochs, with a peak-to-valley excursion of 0.52 in the Y band and about 0.4 and 0.5 mag in the J and H band. It is not clear if this is a real effect or an artifact of our reductions. Since we worked differentially with respect to the primary, we should take into consideration the possibility that this is a variable star. Primary variability was noted by Biller et al. (2012), who reported a significant variation between the 2MASS photometry and the Malfait et al. (1998) photometry. HD142527 is a Herbig Ae object that is listed as probable δ Scuti pulsator in Marconi & Palla (1998). However, Kurtz & Müller (2001) did not find any δ Scuti pulsation, but a stellar variability with a period of about 6.0 d. We observed the star[2] (Messina & Millward, 2017 Priv. Comm.) from April 2017 to August 2017 for a total of 13 nights, confirming the period of 6.0 d with a peak-to-valley amplitude of 0.13 mag in B and 0.09 mag in V and R. We conclude that the photometric variability amplitude of the primary is not sufficient to explain the amplitude of the variation we found in our observation of B. On the other hand, in an extensive NIR photometrical study of the RCW38 star-forming region, Dörr et al. (2013) found that most of the low-mass stars in their sample exhibit irregular light curves with typical timescales of a few days and amplitudes between 0.1 and 0.4 mag in K band. Some of them show variations and outbursts with amplitudes above 1 mag. If this is the case for HD142527B, as it may be because its very young age (1.0 - 5.0 Myr), the variable behavior of NIR photometry of young stars can most likely explain the photometrical variation shown in Table 2.

[2] At the York Creek Observatory, Georgetown, Australia

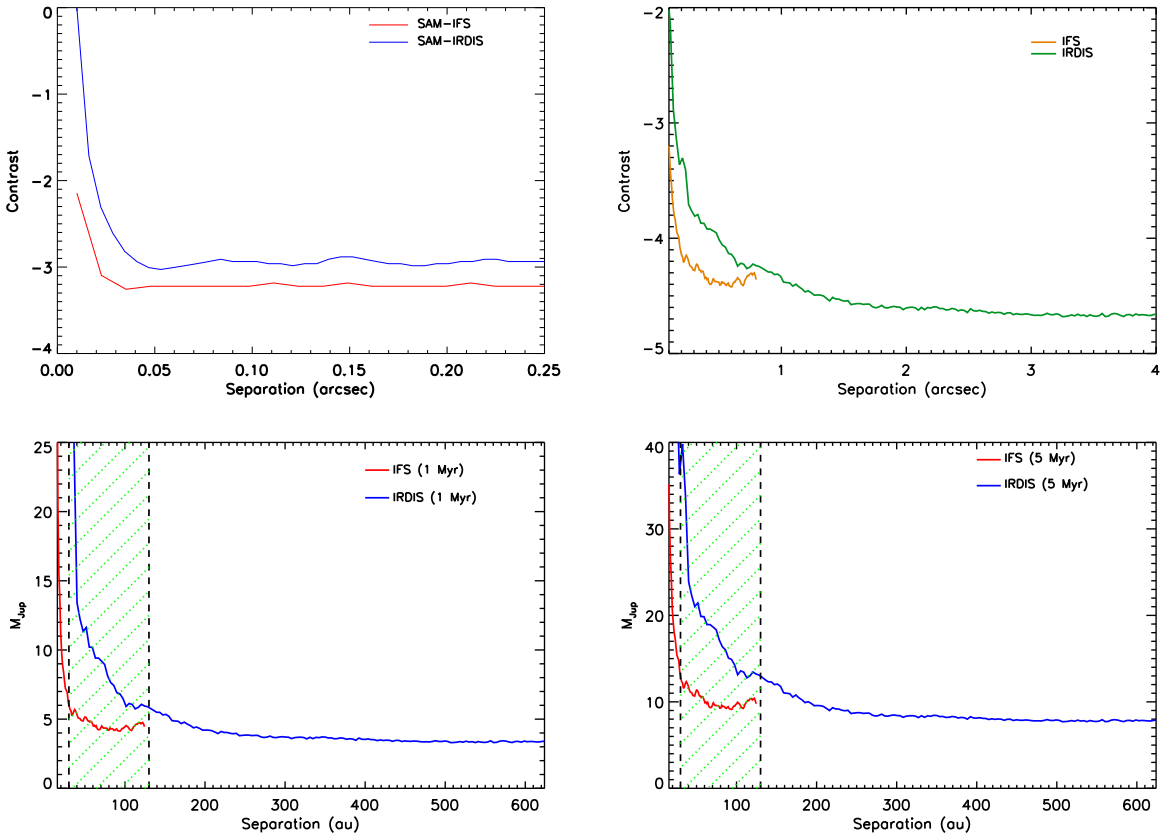

Fig. 4. Top left: IFS and IRDIS contrast limits achieved within 250 mas using the SAM observing mode. **Top right**: IFS and IRDIS contrast limits achieved during the non-coronagraphic observations of HD142527. **Bottom left**: Minimum detectable mass as a function of separation in the field of view of IFS and IRDIS, adopting an age of 1 Myr and the models of BHAC2015. **Bottom right**: Minimum detectable mass as a function of separation, adopting an age of 5 Myr. The shaded area between the two dashed vertical lines indicates the disk gap as reported by Verhoeff et al. (2011).

5.3. Astrometry

To precisely determine the position of the companion from the IFS images taken at different observing epochs, we inserted negative-simulated companions (built from a 2D Gaussian function) at different positions around the position of the true companion. The best fit to this position was found from the position of the negative simulated companion, which minimized the standard deviation in the region around it. The results for each epoch are listed in Table 4. Since the observations are non-coronagraphic, the position of the primary star could be defined with high precision because its signal is strong and unbiased. This shows that the dominant source of uncertainty remains the centering of the secondary star, which is assumed to be accurate to half of a pixel scale. The main contribution to the error on the position angle is dominated by the uncertainty on the true north (TN) angle, calculated by observing an astrometric calibration field (Maire et al. 2016).

5.4. Detection limits

The best limiting contrast curves as a function of separation obtained for both IFS and IRDIS (see Mesa et al. (2015)) for a complete description of the method we used to evaluate the limiting contrast curves) are shown in the upper panels of Figure 4. Here we also show the best limiting contrast curve obtained with the SAM observing mode for IRDIS and IFS for separations smaller than 250 mas (39 au). The lower panel shows the minimum detectable mass as a function of separation in the field of view (FoV) of IFS and IRDIS. In the figure, the inner and outer limits of the disk gap are also highlighted with vertical dashed lines. We considered the mass limits for ages of 5 Myr, as stated for HD142527 by Fukagawa et al. (2006), and of 1 Myr, which resulted from comparing the photometry of HD142527B with models from Baraffe et al. (2015, henceforth BHAC 2015) (see Section 6.1). The non-coronagraphic setup that was used for the observations means that the achieved contrast at sep $\geq$ 0.7 arcsec is lower than the contrast achieved in coronagraphic observations. The less favorable pixel scale of the IRDIS observations and the proximity of HD142527B to the central star produce lower contrasts at small separations than in the IFS performance. For the IFS FoV, we reach minimum detectable companion masses of 7 − 10 M_J (depending on the age of the system). Boehler et al. (2017), in their analysis of ALMA observations of HD142527, found a compact source in the continuum map as well as CO emission at about 50 au from the central star. They interpreted this as material orbiting a low-mass companion. Except for HD142527B, we detect no companion with a mass higher than 10 M_J orbiting HD142527 in the large gap between the inner and the circumbinary disks. Consequently, the third object in the system proposed by Boehler et al. (2017), if it exists, should be less massive than 10 M_J. At larger orbital radii up to 500

Table 4. Astrometric position derived for HD142527B for each individual epoch.

Date	ΔRA (mas)	ΔDec (mas)	Separation (mas)	Position Angle (deg)
2015-05-13	65±2	−24±2	69±2	110.2±0.5
2015-07-03	62.9±0.4	−18.3 ± 0.5	65.5± 0.4	106.2 ± 0.4
2016-03-26	60±2	−7±2	60±2	97.1±0.5
2016-06-13	61±2	−7±2	61±2	96.3±0.5
2017-05-16	47.4 ± 0.5	10.3 ± 0.2	48.5 ± 0.5	77.8 ± 0.2
2018-04-14	36 ± 1	25 ± 1	44 ± 1	55.4 ± 0.4

au (the complete FoV of IRDIS), no planets with masses higher than $3-7$ M_J (depending on the age of the system) are detected.

6. HD142527B mass estimate

The spectroscopic results discussed in Section 5.1 can be used to estimate the mass and radius of HD142527B. The analysis of Pecaut & Mamajek (2013) on cool pre-main-sequence stars also provides a tentative determination of the mass and radius of such objects based on spectral type. Our determination of the spectral type yields a value of M = $0.11^{+0.04}_{-0.02}$ $M_\odot$ and R= $0.15^{+0.07}_{-0.01}$ $R_\odot$.

6.1. Comparison to evolutionary models

The mass, radius, and age of this star can be obtained by comparisons between the measured absolute magnitudes and model absolute magnitudes from theoretical evolutionary tracks. In this case, we considered the standard evolutionary models of BHAC 2015. In Figure 5 we display the isochrones for models with masses ranging between 0.05 $M_\odot$ to 0.80 $M_\odot$ and for ages between 0.5 Myr to 8 Myr, on which we overlay the observed points (blue dots) at different epochs and their average. A suitable set of parameters for this comparison is M= 0.14 ± 0.03 $M_\odot$, R= 1.2 ± 0.5 $R_\odot$, and an age of about 1 Myr. Although this mass determination agrees with our previous estimate based on spectroscopic data and with the result reported in Lacour et al. (2016), it is most likely not conclusive. The absolute magnitudes of HD142527B are systematically too bright compared to the models. This is mainly due to the accretion of matter onto this young star (Close et al. 2014) that is not taken into account in the evolutionary tracks of structures, which instead only account for gravitational contraction. The accretion produces a hotter object with a larger radius. We tried to account for the contribution of the disk (see Section 5.2), but other effects can contribute to the luminosity of the secondary, such as the inner disk. It is expected that if such effects were accounted for in the isochrones, the points would shift toward larger magnitudes. If we were to take the higher temperature and brighter absolute magnitude that is due to accretion into account in the model, the isochrone system would move mainly parallel to the arrow in the Figure 5, rendering this analysis inconclusive.

6.2. Dynamical constraints

An alternative and promising way to constrain the mass of HD142527B is to evaluate the proper motion variation of the primary star that is due to the presence of the secondary. To this purpose, we searched for significant differences in proper motion of the star as measured at different epochs (see Table 5). HD142527 is present in several catalogs, and the comparison of GAIA and Tycho2 (Høg et al. 2000) proper motions gives $\Delta\mu_\alpha$ = (2.14 ± 1.00) mas/yr and $\Delta\mu_\delta$ = (1.04 ± 1.00) mas/yr. The

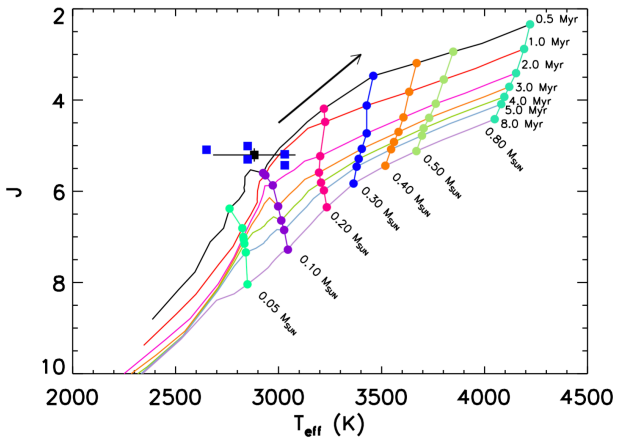

Fig. 5. Evolutionary tracks and isocontours of masses as function of the temperature and absolute magnitude J as evaluated in BAHC 2015 The blue squares are the observed absolute magnitudes of HD142527B corrected for the contribution due to the circum-secondary disk, and the black square is their mean with error bars. The arrow qualitatively indicates how the isochrone system would change with respect to the observed points if the accretion process is taken into account in the models.

GAIA and SPM (Girard et al. 2011, Southern Proper Motion Catalogue) $\Delta\mu_\alpha$ = (2.40 ± 3.40) mas/yr and $\Delta\mu_\delta$ = (9.68 ± 3.26) mas/yr and GAIA and UCAC5 (Zacharias et al. 2017) $\Delta\mu_\alpha$ = (1.44 ± 1.9) mas/yr and $\Delta\mu_\delta$ = (0.34 ± 1.90) mas/yr also show significant differences in proper motion.

We were therefore able to use the code for orbital parametrization of astrometrically identified new systems (COPAINS, Fontanive et al. in prep.) to evaluate the characteristics of the possible companions that are compatible with the observed $\Delta\mu$. The code uses Eq. 1 from Makarov & Kaplan (2005), derived by Makarov & Kaplan (2005), to estimate the change in a stellar proper motion that is induced by a companion for a range of possible masses and separations,

$$\Delta\mu \leq \frac{2\pi\Pi R_0 M_2}{\sqrt{a M_{Tot}}}. \quad (1)$$

where, M_2 is the mass of the secondary, M_{Tot} is the total mass of the binary, a is the semi-major axis in AU, Π is the parallax of the system in mas, and R_0 takes into account the orbital phase so that $R_0 = \left(\frac{1+e\cos E}{1-e\cos E}\right)^{1/2}$, where e is the orbital eccentricity and E is the eccentric anomaly. A fine grid of mass and separation values is explored, and the expected $\Delta\mu$ is evaluated and compared with the observed one. In order to properly take into account the projection effects, the code considers for each point on the mass-separation grid 10^6 possible orbital configurations,

Table 5. Values for different catalogs and epochs of the HD142527 proper motion.

Catalog	μ_α mas/yr	$\delta\mu_\alpha$ mas/yr	μ_δ mas/yr	$\delta\mu_\delta$ mas/yr	p mas	δp mas	Epoch yr
TGAS[a]	−11.76	0.08	−24.46	0.05	6.40	0.26	2015.00
Hipparcos New	−11.19	0.93	−24.46	0.79	4.29	0.98	1991.25
Tycho2	−13.9	1.00	−25.5	1.0			1991.02
SPM 4.0	−14.16	3.42	−14.78	3.26			2006.12
UCAC5[b]	−13.2	1.9	−24.8	1.9			1998.50

[a] Tycho – GAIA Astrometric Solution
[b] Fifth US Naval Observatory Astrograph Catalog

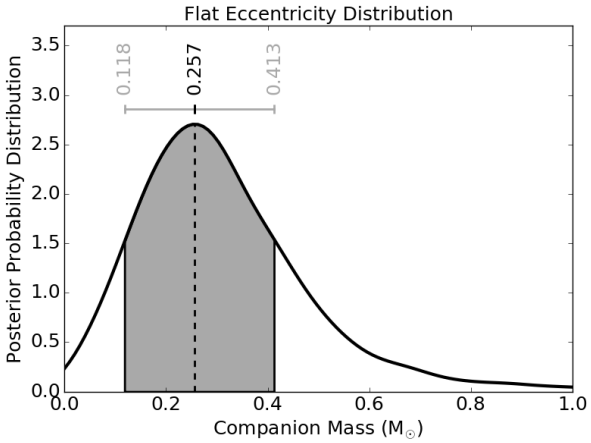

Fig. 6. Mass distribution, obtained using the COPAINS, of the companions that are compatible with the observed $\Delta\mu$ for HD142527, at a physical separation that is compatible with the SPHERE detection. The dashed line shows the position of the most likely value, and the shaded area highlights the region within a 1 σ confidence level.

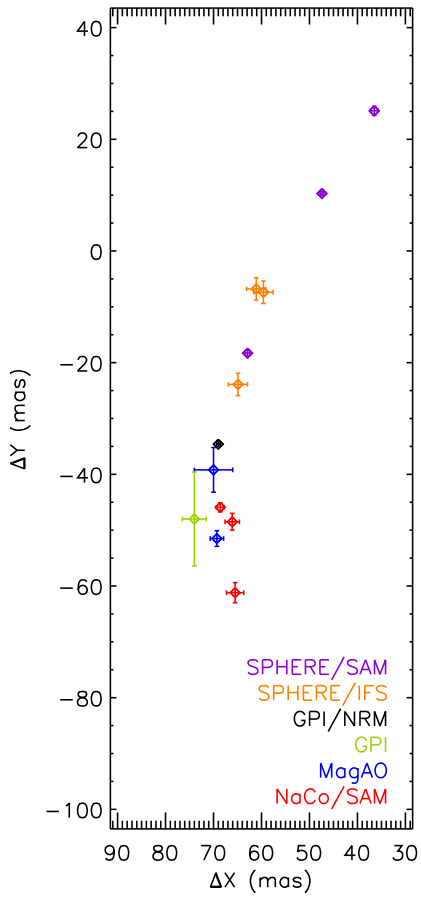

Fig. 7. Astrometric measurements of HD142527B from the literature (NaCo, MagAO, and GPI data) and this work (SPHERE data). The GPI measurement (green data point) is shown for comparison, but is not used in the analysis (see text).

with eccentricities drawn from a uniform distribution (a Gaussian distribution can also be used, see Bonavita et al. (2016) for further details and other applications of the code).

If an estimate of the orbital parameters is available, as in the case of HD142527B (see Section 7 for the details of the orbital characterization), the code allows us to retrieve the mass distribution for companions compatible with the observed trend and the orbital characteristics. Figure 6 shows the results of the application of this method to HD142527B. The retrieved mass distribution peaks at $0.26^{+0.16}_{-0.14}$ $M_\odot$ and is therefore compatible with the value obtained in the analysis based on the spectral classification and the calibration by Pecaut & Mamajek (2013) discussed at the beginning of this section.

7. Orbital properties of HD142527B

We combined the astrometric measurements of the companion reported in the literature (Close et al. 2014; Rodigas et al. 2014; Lacour et al. 2016) with the new SPHERE/IFS and SPHERE/SAM measurements (Table 4) to perform a new orbital study. The measurements are shown in Fig. 7. We show the GPI polarimetric differential imaging measurement in Rodigas et al. (2014) for comparison, but we did not use it for our analysis because of its large uncertainties and because a more accurate GPI SAM measurement close in time is available from Lacour et al. (2016). The SPHERE data represent an increase by almost a factor 3 in the observational baseline with respect to the previous study of Lacour et al. (2016). In about four years, the position angle of the companion decreased by ∼61° and its separation decreased by ∼33 mas. The data in Fig. 7 indicate inflections in both separation and position angle in the orbital motion of the companion. We show the evolution of the separation and position angle of the companion as a function of time in Fig. 8. The separation and position angle measured in 2018 deviate from a linear trend based on the data points listed in Lacour et al. (2016) at a significance of ∼8 and 73 σ, respectively. In addition, the companion separation decreases. We therefore conclude that the companion is accelerating on its orbit and approaches its periapsis.

We used a least-squares Monte Carlo (LSMC) algorithm to fit the astrometric measurements and derive distributions of the

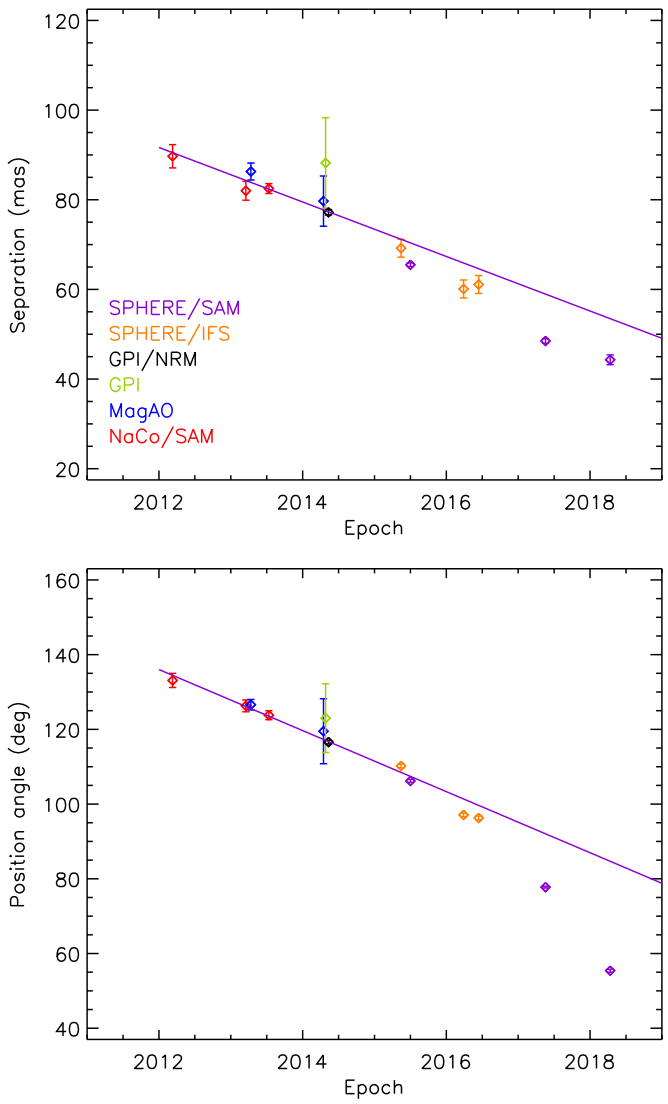

Fig. 8. Temporal evolution of the separation (*top*) and position angle (*bottom*) of HD142527B. For both panels, a linear fit to the data points obtained before 2015 is shown (purple solid line) to show the progressive deviation from linearity of the SPHERE measurements. The GPI measurements (green data points) are not considered for the fits.

orbital parameters. The approach has previously been described in Esposito et al. (2013) and Maire et al. (2015). We assumed a distance for the system of 156 pc (Gaia Collaboration et al. 2016) and a total system mass of 2.1 $M_{\odot}$ (Lacour et al. 2016). We drew 2 000 000 random realizations of the astrometric measurements assuming Gaussian distributions around the nominal values. Then, we fit the six Campbell elements simultaneously using a debugged version of the downhill simplex `AMOEBA` algorithm[3] (Eastman et al. 2013). Initial guesses for the orbital elements were drawn assuming uniform distributions. We considered no priors on the orbital elements, except for the period (P=10–2000 yr). Figure 9 shows the histogram distributions of the orbital parameters for all the derived solutions with $\chi^2_{\rm red} < 2$. The 68% intervals for the parameters are orbital period $P = 35$–137 yr, inclination $i = 121$–130°, longitude of node $\Omega \sim 124$–135°, and argument of periapsis $\omega = 44$–117°. For the eccentricity and time at periapsis passage, each distribution exhibits two groups of possible values: ~0.2–0.45 and ~0.45–0.7 for e, and ~2015–2020 and ~2020–2022 for T_0.

The shape of the distributions of the orbital parameters are broadly consistent with those derived in Lacour et al. (2016) using a Markov chain Monte Carlo algorithm for the parameters in common, except that all the solutions are consistent with a companion approaching its periapsis passage. Some parameters are better constrained by our updated analysis (inclination, longitude of node, and argument of periapsis), whereas others have larger ranges (period). The latest data points probe very close to the periapsis passage, hence we cannot firmly conclude whether the companion has passed it. Further monitoring is required to address this point. Lacour et al. (2016) found two families of orbital solutions, where the companion approaches periapsis in one case and has recently past periapsis in the other case. They were not able to distinguish between these two solutions because available data offer only small orbital coverage and the evolution of the separation and position angle with time does not deviate from linearity. Figure 10 shows the predicted separations and position angles for all the orbital solutions derived in our analysis. The position angle (PA) decrease will continue in the coming years with a high variation rate, while the separation will reach minimum before increasing again starting from ~2019. Astrometric follow-up of the companion will be critical to precisely determine the time and separation at its periapsis passage.

The right panel of Fig.10 represents the fitted orbits projected on the plane of the sky. The inset shows a zoom around the astrometric measurements. In the main panel we also indicate with different colors three representative orbits among the orbital solutions. The orbits similar to the orbit shown in blue compose the largest group of all three groups (~77% of all fitted orbits). They are characterized by a longitude of node larger than 100° and periods longer than ~40 yr. The orbits represented by the orbit marked in red are the second largest group (~22% of all fitted orbits) and have longitudes of node larger than 100° , but periods shorter than 40 yr. Finally, there is a small group of orbits shown by the orbit colored in green (~0.22%) with periods longer than ~40 yr, but longitudes of node smaller than 100°. These three types of orbits also have different times at periastron passages, the first group have T_0 before ~2019, the second group around 2019.5, and the last group after after ~2020. The plot shows that they quickly diverge after the last measurement, so that further astrometric measurements in the coming years will provide strong constraints for distinguishing between these orbits.

The distributions of separations at apoapsis and periapsis from our LSMC analysis shown in the left panel of Fig. 11 indicate a range at 68% ~18–57 au. If the companion is coplanar with the outer disk, a ~0.25-$M_{\odot}$ companion with a 50 au apoapsis and $e \sim 0.5 - 0.7$ would in principle create a region of orbital instability extending out to ~ 100 au (Holman & Wiegert 1999), which is the innermost possible location for the outer disk (e.g., Fukagawa et al. 2006; Casassus et al. 2012; Rameau et al. 2012; Rodigas et al. 2014; Avenhaus et al. 2017). Nevertheless, the inclination and longitude of node of HD142527B disagree with those of the outer circumstellar disk (i=28°, Ω=160°, Verhoeff et al. 2011; Perez et al. 2015), as has been reported by Lacour et al. (2016). This result would at first sight rule out that HD142527B is responsible for the outer disk truncation. However, recent hydrodynamical simulations have shown that for an eccentric companion with an almost polar inclination to the outer disk that approaches its periapsis passage, the interactions of

[3] The customized built-in routine provided by IDL truncates the stepping scales to floating point precision, regardless of the type of input data.

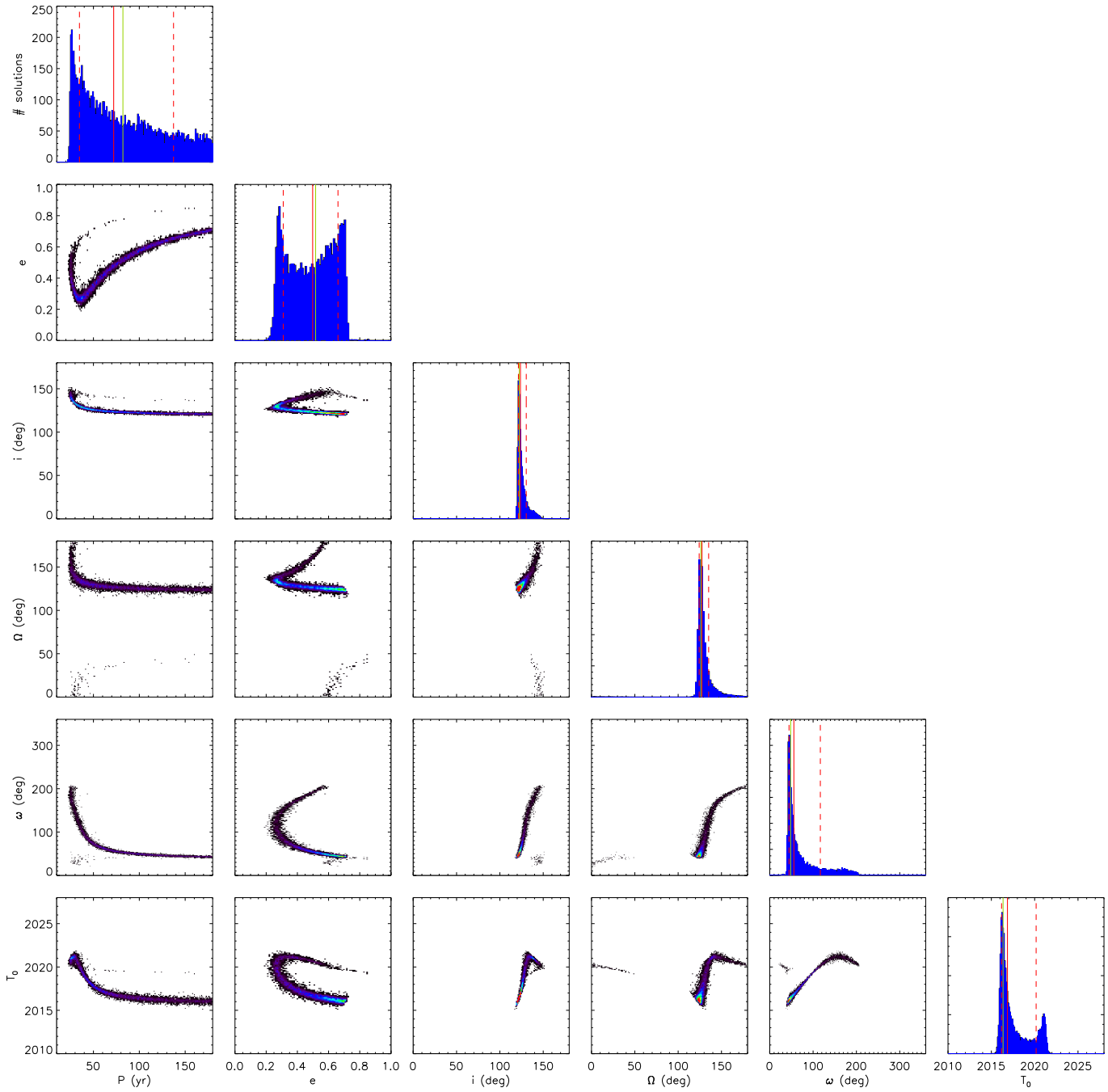

Fig. 9. LSMC distributions of the six Campbell orbital elements for all the fitted solutions with $\chi^2_{\rm red} < 2$ among 2 000 000 random trials. The diagonal diagrams represent the 1D histogram distributions of the individual elements. The off-diagonal diagrams show the correlations between pairs of orbital elements. The linear color scale in the correlation plots accounts for the relative local density of the orbital solutions. In the diagonal histograms, the red solid line represents the 50 percentile values, the red dashed lines show the intervals at 68%, and the green solid line indicates the best χ^2 fitted solution.

companion and disk can reproduce several of the main observed disk features, such as its large cavity, and with the correct position angles, its spiral features and shadows (Price et al. 2018). This orbital configuration is broadly consistent with the results from our orbital analysis. On the other hand, the orbital plane of the companion is close to the plane of the inner circumstellar disk, as previously suggested by Lacour et al. (2016). The inner disk has a position angle of 110±10° from CO(6-5) kinematics measured with ALMA (Casassus et al. 2015). Its mean radius is estimated to be about 10 au from near-infrared interferometric observations (Anthonioz et al., in prep.). From MIR imaging and SED modeling, Verhoeff et al. (2011) derived a maximum radial extension for the inner disk up to 30 au. However, Avenhaus et al. (2014) imaged the inner circumstellar environment down to ~0.1″ (15 au) in polarized scattered light with NaCo, but did not detect traces of an inner disk. More recently, Avenhaus et al. (2017) imaged the disk in visible polarized light with SPHERE down to 25 mas (~4 au) and found evidence for dust scattering close to the star, although it remains unclear if this scattering is related to the inner disk because of geometrical discrepancies

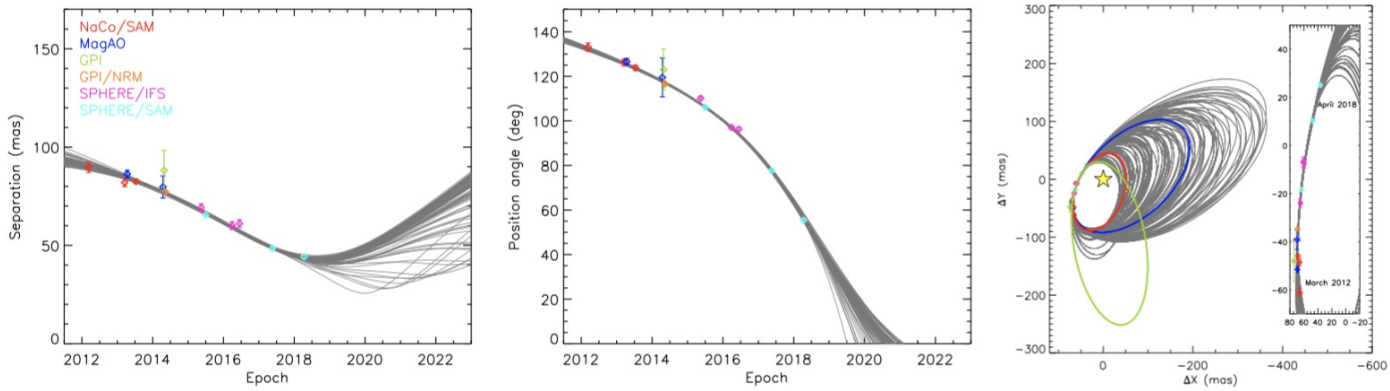

Fig. 10. Predicted separations (*left*), position angles (*middle*), and sky-plane positions (*right*) for the subset of 100 randomly selected orbital solutions shown in Fig. 9. In the right panel we also show with different colors three representative orbits among the fitted solutions (see text) and an inset providing a zoom around the region that is covered by the data points.

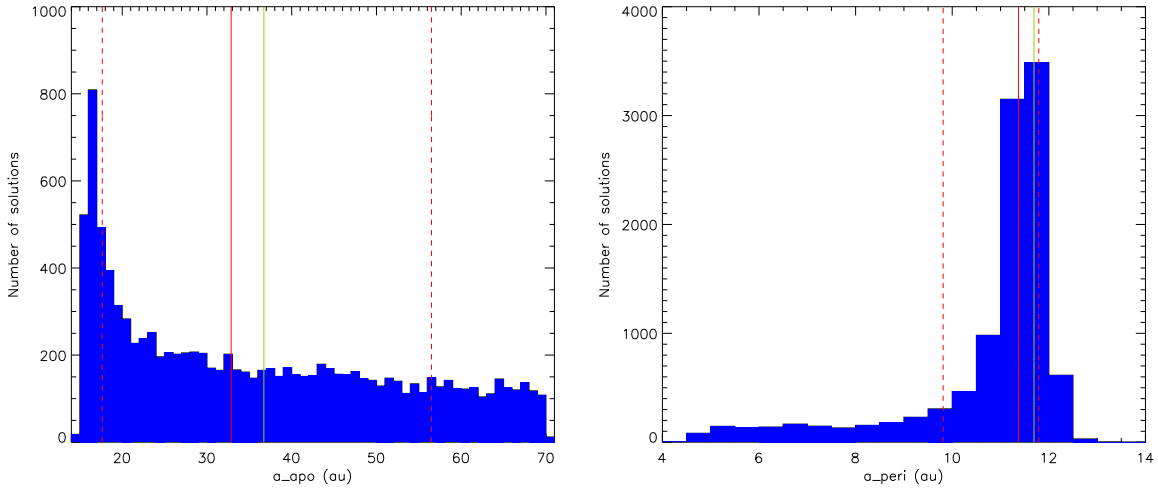

Fig. 11. Same as the diagonal plots in Fig. 9, but for the separation at apoapsis (left) and periapsis (right).

with predictions from a modeling of the shadows projected onto the outer disk (Marino et al. 2015). Using our orbital analysis of the companion, we derived the distribution of its separation at periapsis (Fig. 11, right panel) and find a 68% confidence interval of $\sim 10 - 12$ au. This results indicates that the shape of the inner disk is strongly affected by HD142527B.

8. Discussion and conclusion

We here presented a detailed characterization of the stellar companion of HD142527. We refined the previously estimated spectral and orbital characteristics of HD142527B using IFS low-resolution spectra in both IRDIFS_EXT observing mode and also using the SAM technique without a coronagraph. Because the observations were taken in non-coronagraphic mode, the IRDIS images taken in IRDIFS_EXT mode were used not for photometry, but only to detect the mass limit. Except for HD142527B, we detect no objects with masses greater than 10 M_J inside the gap of the disk, based on our achieved IFS contrasts. This constrains the mass of the third object hypothesized by Boehler et al. (2017) at 50 au from the central star to lower than 10 M_J. The images obtained with IRDIS exclude the presence of planets with masses greater than 7 M_J up to 500 au. However, the non-coronagraphic technique we used in our observations means that the achieved contrast at sep $\geq$ 0.7 arcsec is lower than is typically achieved in coronagraphic SPHERE images. A better mass limit outside and inside the IFS FoV will be obtained with future SPHERE coronagraphic observations.

Our results confirm that HD142527B is an M star with a spectral type of M5-M7 and a T_{eff} between 3030 and 2650 K. The spectra are variable in flux because of several possible factors, such as 1) the variation in stellar temperature, or 2) the contribution from the accretion disk around the secondary, and/or 3) the variation in circumstellar material absorption (around the primary or secondary, or around both) that is due to interaction with the environment and to the young age of the system. In comparing the absolute magnitude of the B component to the models, we find (like Lacour et al. (2016)) that the age of the secondary is very young ($\sim$ 1 Myr), younger than the age of the primary (5 Myr). In order to match the same age for the companion as for the A component and to make this agree with the evolutionary tracks in Figure 5, we would have to add about 2.0 mag to the J magnitude, pushing the system to a distance of about 62 pc, which is not compatible with the distance measured by Gaia Collaboration et al. (2016), as reported in Section 2. As described in Section 6.1, this discrepancy arises because accretion is not taken into account in the young-object models. This accretion will cause the object to appear younger and redder than a non-accreting object. Because of these caveats, we consider the comparison to the theoretical models of young objects inconclusive. This means that the spectral type of the secondary star may also be earlier than M6. By studying the proper motion of the primary

star, we dynamically constrained the mass of the secondary to be $M_{HD142527B} = 0.26^{+0.16}_{-0.14}$ $M_\odot$. This value is in agreement with our spectroscopic estimate (see Section 6) and with the estimate of Lacour et al. (2016). Following Pecaut & Mamajek (2013) the lower and upper dynamical mass values correspond to a spectral type between M2.5 and M5.5. To our knowledge, this is the first dynamical mass determination for HD142527B that was made by exploiting the difference between nearly instantaneous and long-term motion. Significant improvements are expected after the full *GAIA* dataset is available.

By combining the new SPHERE/IFS and SPHERE/SAM astrometric measurements with those reported in the literature, we constrained the orbital properties of HD142527B and obtained a period of P= 35−137 yr, an inclination of $i = 121-130°$ degrees, a value of $\Omega = 124-135°$ degrees for the longitude of node, and an 68% confidence interval of $\sim 18-57$ au for the separation at periapsis. Eccentricity and time at periapsis passage exhibit two groups of values: ∼0.2–0.45 and ∼0.45–0.7 for e, and ∼2015–2020 and ∼2020–2022 for T_0. The orbit of the secondary is more inclined than the outer circumstellar disk and seems to rule out that HD142527B is responsible for the truncation of the outer disk. On the other hand, these results are also consistent with the scenario described by Price et al. (2018), in which a companion close to its periapsis in an eccentric and highly inclined orbit with respect to the outer disk could be responsible for the large cavity and other observed features and shadows. Our distribution of the orbital parameters are in good agreement with those of Lacour et al. (2016). Our solutions are consistent with a companion that is approaching its periapsis passage, but the errors on our derived eccentricity and period are too large (but further monitoring is required) to conclusively determine whether the companion has passed periapsis. The next two or three years of observations will be crucial to clarify this point.

Acknowledgements. SPHERE is an instrument designed and built by a consortium consisting of IPAG (Grenoble, France), MPIA (Heidelberg, Germany), LAM (Marseille, France), LESIA (Paris, France), Laboratoire Lagrange (Nice, France), INAF–Osservatorio di Padova (Italy), Observatoire de Genève (Switzerland), ETH Zurich (Switzerland), NOVA (Netherlands), ONERA (France) and ASTRON (Netherlands) in collaboration with ESO. SPHERE was funded by ESO, with additional contributions from CNRS (France), MPIA (Germany), INAF (Italy), FINES (Switzerland) and NOVA (Netherlands). SPHERE also received funding from the European Commission Sixth and Seventh Framework Programmes as part of the Optical Infrared Coordination Network for Astronomy (OPTICON) under grant number RII3–Ct–2004–001566 for FP6 (2004–2008), grant number 226604 for FP7 (2009–2012) and grant number 312430 for FP7 (2013–2016). This work has made use of the SPHERE Data Centre, jointly operated by Osug/Ipag (Grenoble), Pytheas/Lam/Cesam (Marseille), OCA/Lagrange (Nice) and Observatoire de Paris/Lesia (Paris) and supported by a grant from Labex OSUG@2020 (Investissements d'avenir ANR10 LABX56). This work has been in particular carried out in the frame of the National Centre for Competence in Research 'PlanetS' supported by the Swiss National Science Foundation (SNSF). D.M. acknowledges support from the ESO-Government of Chile Joint Comittee program "Direct imaging and characterization of exoplanets". A.Z. acknowledges support from the CONICYT + PAI/ Convocatoria nacional subvención a la instalación en la academia, convocatoria 2017 + Folio PAI77170087. J. O. acknowledges support from the ICM (Iniciativa Científica Milenio) via the Nucleo Milenio de Formación planetaria grant, from the Universidad de Valparaíso and from Fondecyt (grant 1180395).

References

Acke, B. & van den Ancker, M. E. 2004, A&A, 426, 151
Allard, F. 2014, in IAU Symposium, Vol. 299, Exploring the Formation and Evolution of Planetary Systems, ed. M. Booth, B. C. Matthews, & J. R. Graham, 271–272
Allers, K. N. & Liu, M. C. 2013, ApJ, 772, 79
Antichi, J., Dohlen, K., Gratton, R. G., & et al. 2009, ApJ, 695, 1042
Avenhaus, H., Quanz, S. P., Schmid, H. M., et al. 2017, AJ, 154, 33
Avenhaus, H., Quanz, S. P., Schmid, H. M., et al. 2014, ApJ, 781, 87
Baraffe, I., Homeier, D., Allard, F., & et al. 2015, A&A, 577, A42
Beuzit, J.-L., Feldt, M., Dohlen, K., et al. 2008, in Proc. SPIE, Vol. 7014, Ground-based and Airborne Instrumentation for Astronomy II, 701418
Biller, B., Lacour, S., Juhász, A., & et al. 2012, ApJ, 753, L38
Biller, B. A., Males, J., Rodigas, T., & et al. 2014, ApJ, 792, L22
Boccaletti, A., Abe, L., Baudrand, J., & et al. 2008, in Proc. SPIE, Vol. 7015, Adaptive Optics Systems, 70151B
Boehler, Y., Weaver, E., Isella, A., et al. 2017, ApJ, 840, 60
Bonavita, M., Desidera, S., Thalmann, C., et al. 2016, A&A, 593, A38
Brittain, S. D., Carr, J. S., Najita, J. R., Quanz, S. P., & Meyer, M. R. 2014, ApJ, 791, 136
Brittain, S. D., Najita, J. R., Carr, J. S., et al. 2013, ApJ, 767, 159
Cardelli, J. A., Clayton, G. C., & Mathis, J. S. 1989, ApJ, 345, 245
Casassus, S., Marino, S., Pérez, S., et al. 2015, ApJ, 811, 92
Casassus, S., Perez M., S., Jordán, A., et al. 2012, ApJ, 754, L31
Casassus, S., van der Plas, G., M, S. P., & et al. 2013, Nature, 493, 191
Chauvin, G., Desidera, S., Lagrange, A.-M., et al. 2017, in SF2A-2017: Proceedings of the Annual meeting of the French Society of Astronomy and Astrophysics, ed. C. Reylé, P. Di Matteo, F. Herpin, E. Lagadec, A. Lançon, Z. Meliani, & F. Royer, 331–335
Cheetham, A. C., Girard, J., Lacour, S., et al. 2016, in Proc. SPIE, Vol. 9907, Optical and Infrared Interferometry and Imaging V, 99072T
Claudi, R., Antichi, J., Baruffolo, A., et al. 2016, in Proc. SPIE, Vol. 9908, Ground-based and Airborne Instrumentation for Astronomy VI, 99083H
Claudi, R. U., Turatto, M., Gratton, R. G., & et al. 2008, in Proc. SPIE, Vol. 7014, Ground-based and Airborne Instrumentation for Astronomy II, 70143E
Close, L. M., Follette, K. B., Males, J. R., & et al. 2014, ApJ, 781, L30
Cutri, R. M., Skrutskie, M. F., van Dyk, S., et al. 2003, VizieR Online Data Catalog, 2246
Delorme, P., Meunier, N., Albert, D., et al. 2017, in SF2A-2017: Proceedings of the Annual meeting of the French Society of Astronomy and Astrophysics, ed. C. Reylé, P. Di Matteo, F. Herpin, E. Lagadec, A. Lançon, Z. Meliani, & F. Royer, 347–361
Dodson-Robinson, S. E. & Salyk, C. 2011, ApJ, 738, 131
Dohlen, K., Langlois, M., Saisse, M., & et al. 2008, in Proc. SPIE, Vol. 7014, Ground-based and Airborne Instrumentation for Astronomy II, 70143L
Dörr, M., Chini, R., Haas, M., Lemke, R., & Nürnberger, D. 2013, A&A, 553, A48
Eastman, J., Gaudi, B. S., & Agol, E. 2013, PASP, 125, 83
Espaillat, C., Muzerolle, J., Najita, J., & et al. 2014, Protostars and Planets VI, 497
Esposito, S., Mesa, D., Skemer, A., et al. 2013, A&A, 549, A52
Fedele, D., Carney, M., Hogerheijde, M. R., et al. 2017, A&A, 600, A72
Foreman-Mackey, D., Hogg, D. W., Lang, D., & Goodman, J. 2013, PASP, 125, 306
Fukagawa, M., Tamura, M., Itoh, Y., et al. 2006, ApJ, 636, L153
Fukagawa, M., Tsukagoshi, T., Momose, M., & et al. 2013, PASJ, 65, L14
Fusco, T., Sauvage, J.-F., Petit, C., et al. 2014, in Proc. SPIE, Vol. 9148, Adaptive Optics Systems IV, 91481U
Gaia Collaboration, Brown, A. G. A., Vallenari, A., et al. 2016, A&A, 595, A2
Garcia Lopez, R., Natta, A., Testi, L., & Habart, E. 2006, A&A, 459, 837
Girard, T. M., van Altena, W. F., Zacharias, N., et al. 2011, AJ, 142, 15
Greenbaum, A. Z., Cheetham, A., Sivaramakrishnan, A., & et al. 2014, in Proc. SPIE, Vol. 9147, Ground-based and Airborne Instrumentation for Astronomy V, 91477B
Henize, K. G. 1976, ApJS, 30, 491
Høg, E., Fabricius, C., Makarov, V. V., et al. 2000, A&A, 355, L27
Holman, M. J. & Wiegert, P. A. 1999, AJ, 117, 621
Houk, N. 1978, Michigan catalogue of two-dimensional spectral types for the HD stars
Hugot, E., Ferrari, M., El Hadi, K., & et al. 2012, A&A, 538, A139
Jovanovic, N., Guyon, O., Lozi, J., et al. 2016, in Proc. SPIE, Vol. 9909, Adaptive Optics Systems V, 99090W
Kraus, A. L. & Ireland, M. J. 2012, ApJ, 745, 5
Kraus, A. L., Ireland, M. J., Martinache, F., & Lloyd, J. P. 2008, ApJ, 679, 762
Kurtz, D. W. & Müller, M. 2001, MNRAS, 325, 1341
Lacour, S., Biller, B., Cheetham, A., et al. 2016, A&A, 590, A90
Langlois, M., Vigan, A., Moutou, C., et al. 2013, in Proceedings of the Third AO4ELT Conference, ed. S. Esposito & L. Fini, 63
Ligi, R., Vigan, A., Gratton, R., et al. 2018, MNRAS, 473, 1774
Macintosh, B. A., Anthony, A., Atwood, J., et al. 2014, in Proc. SPIE, Vol. 9148, Adaptive Optics Systems IV, 91480J
Maire, A.-L., Langlois, M., Dohlen, K., et al. 2016, in Proc. SPIE, Vol. 9908, Ground-based and Airborne Instrumentation for Astronomy VI, 990834
Maire, A.-L., Skemer, A. J., Hinz, P. M., et al. 2015, A&A, 576, A133
Makarov, V. V. & Kaplan, G. H. 2005, AJ, 129, 2420
Malfait, K., Bogaert, E., & Waelkens, C. 1998, A&A, 331, 211
Malfait, K., Waelkens, C., Bouwman, J., & et al. 1999, A&A, 345, 181
Marconi, M. & Palla, F. 1998, ApJ, 507, L141
Marino, S., Perez, S., & Casassus, S. 2015, ApJ, 798, L44

Marois, C., Correia, C., Galicher, R., et al. 2014, in Proc. SPIE, Vol. 9148, Adaptive Optics Systems IV, 91480U
Marois, C., Lafrenière, D., Doyon, R., & et al. 2006a, ApJ, 641, 556
Marois, C., Lafrenière, D., Macintosh, B., & Doyon, R. 2006b, ApJ, 647, 612
Mendigutía, I., Fairlamb, J., Montesinos, B., & et al. 2014, ApJ, 790, 21
Mesa, D., Gratton, R., Zurlo, A., et al. 2015, A&A, 576, A121
Mordasini, C., Mollière, P., Dittkrist, K.-M., Jin, S., & Alibert, Y. 2015, International Journal of Astrobiology, 14, 201
Mulders, G. D., Min, M., Dominik, C., Debes, J. H., & Schneider, G. 2013, A&A, 549, A112
Muto, T., Grady, C. A., Hashimoto, J., & et al. 2012, ApJ, 748, L22
Osorio, M., Anglada, G., Carrasco-González, C., et al. 2014, ApJ, 791, L36
Pavlov, A., Möller-Nilsson, O., Feldt, M., & et al. 2008, in Proc. SPIE, Vol. 7019, Advanced Software and Control for Astronomy II, 701939
Pecaut, M. J. & Mamajek, E. E. 2013, ApJS, 208, 9
Perez, S., Casassus, S., Ménard, F., et al. 2015, ApJ, 798, 85
Petit, C., Sauvage, J.-F., Fusco, T., & et al. 2014, in Proc. SPIE, Vol. 9148, Adaptive Optics Systems IV, 91480O
Price, D. J., Cuello, N., Pinte, C., et al. 2018, MNRAS, 477, 1270
Quanz, S. P., Amara, A., Meyer, M. R., et al. 2015, ApJ, 807, 64
Quanz, S. P., Amara, A., Meyer, M. R., et al. 2013, ApJ, 766, L1
Rameau, J., Chauvin, G., Lagrange, A.-M., et al. 2012, A&A, 546, A24
Reggiani, M., Christiaens, V., Absil, O., et al. 2017, ArXiv e-prints [arXiv:1710.11393]
Reggiani, M., Quanz, S. P., Meyer, M. R., et al. 2014, ApJ, 792, L23
Rodigas, T. J., Follette, K. B., Weinberger, A., Close, L., & Hines, D. C. 2014, ApJ, 791, L37
Sallum, S., Follette, K. B., Eisner, J. A., et al. 2015, Nature, 527, 342
Salyk, C., Herczeg, G. J., Brown, J. M., & et al. 2013, ApJ, 769, 21
Sissa, E., Gratton, R., Garufi, A., et al. 2018, ArXiv e-prints [arXiv:1809.01001]
Sivaramakrishnan, A. & Oppenheimer, B. R. 2006, ApJ, 647, 620
Soummer, R. 2005, ApJ, 618, L161
Soummer, R., Pueyo, L., & Larkin, J. 2012, ApJ, 755, L28
Strom, K. M., Strom, S. E., Edwards, S., Cabrit, S., & Skrutskie, M. F. 1989, AJ, 97, 1451
Thalmann, C., Schmid, H. M., Boccaletti, A., & et al. 2008, in Proc. SPIE, Vol. 7014, Ground-based and Airborne Instrumentation for Astronomy II, 70143F
Thiébaut, E. 2008, in Proc. SPIE, Vol. 7013, Optical and Infrared Interferometry, 70131I
Tuthill, P., Lacour, S., Amico, P., & et al. 2010, in Proc. SPIE, Vol. 7735, Ground-based and Airborne Instrumentation for Astronomy III, 77351O
Tuthill, P. G., Monnier, J. D., Danchi, W. C., Wishnow, E. H., & Haniff, C. A. 2000, PASP, 112, 555
van Boekel, R., Min, M., Leinert, C., & et al. 2004, Nature, 432, 479
Verhoeff, A. P., Min, M., Pantin, E., et al. 2011, A&A, 528, A91
Vigan, A., Moutou, C., Langlois, M., & et al. 2010, MNRAS, 407, 71
Waelkens, C., Waters, L. B. F. M., de Graauw, M. S., & et al. 1996, A&A, 315, L245
Weingartner, J. C. & Draine, B. T. 2001, ApJ, 548, 296
Williams, J. P. & Cieza, L. A. 2011, ARA&A, 49, 67
Zacharias, N., Finch, C., & Frouard, J. 2017, AJ, 153, 166
Zhu, Z., Nelson, R. P., Hartmann, L., & et al. 2011, ApJ, 729, 47
Zurlo, A., Vigan, A., Galicher, R., et al. 2016, A&A, 587, A57
Zurlo, A., Vigan, A., Mesa, D., et al. 2014, A&A, 572, A85

[1] INAF – Osservatorio Astronomico di Padova e-mail: riccardo.claudi@oapd.inaf.it
[2] Max Planck Institute for Astronomy, Königstuhl 17, D–69117 Heidelberg, Germany
[3] INCT, Universidad De Atacama, calle Copayapu 485, Copiapó, Atacama, Chile
[4] Geneva Observatory, University of Geneva, Chemin des Maillettes 51, 1290 Versoix, Switzerland
[5] SUPA, Institute for Astronomy, The University of Edinburgh, Royal Observatory, Blackford Hill, Edinburgh, EH9 3HJ, UK
[6] Núcleo de Astronomia, Facultad de Ingeniería, Universidad Diego Portales, Av. Ejercito, Santiago, Chile
[7] Escuela de Ingeniería Industrial, Facultad de Ingeniería y Ciencias, Universidad Diego Portales, Av. Ejercito 441, Santiago, Chile
[8] Aix Marseille Université, CNRS, LAM (Laboratoire d'Astrophysique de Marseille) UMR 7326, 13388 Marseille, France
[9] ETH Zurich, Institute for Astronomy, Wolfgang-Pauli-Str. 27, CH-8093, Zurich, Switzerland
[10] Departamento de Astronomía, Universidad de Chile, Casilla 36-D, Santiago, Chile
[11] Millennium Nucleus "Protoplanetary Disk", Departamento de Astronomía, Universidad de Chile, Casilla 36-D, Santiago, Chile
[12] LESIA, Observatoire de Paris, PSL Research University, CNRS, Sorbonne Universités, UPMC Univ. Paris 06, Univ. Paris Diderot, Sorbonne Paris Cité, 5 place Jules Janssen, 92195 Meudon, France
[13] Univ. Grenoble Alpes, CNRS, IPAG, F-38000, Grenoble, France
[14] INAF - Osservatorio Astronomico di Capodimonte, Salita Moiariello 16, 80131 Napoli, Italy
[15] Unidad Mixta Internacional Franco–Chilena de Astronomia, CNRS/INSU UMI 3386 and Departemento de Astronomía, Universidad de Chile, Casilla 36–D, Santiago, Chile
[16] Space Telescope Science Institute, 3700 San Martin Drive, Baltimore, MD 21218, USA
[17] European Southern Observatory (ESO), Alonso de Córdova 3107, Vitacura, Casilla 19001, Santiago, Chile
[18] Department of Astronomy, Stockholm University, AlbaNova University Center, 106 91 Stockholm, Sweden
[19] Steward Observatory, The University of Arizona, Tucson, AZ 85721
[20] CRAL, UMR 5574, CNRS, Universit de Lyon, Ecole Normale Superior de Lyon, 46 Alle d'Italie, F–69364 Lyon Cedex 07, France
[21] INAF-Catania Astrophysical Observatory, via S. Sofia, 78, 95123, Catania, Italy
[22] York Creek Observatory, Georgetown, 7253, Tasmania, Australia
[23] Department of Astronomy, University of Michigan, 1085 S. University, Ann Arbor, MI 48109
[24] Instituto de Física y Astronomía, Facultad de Ciencias, Universidad de Valparaíso, Av. Gran Bretaña 1111, Playa Ancha, Valparaíso, Chile
[25] Núcleo Milenio Formación Planetaria - NPF, Universidad de Valparaíso, Av. Gran Bretaña 1111, Valparaíso, Chile
[26] Monash Centre for Astrophysics (MoCA) and School of Physivs and Astronomy Monash University, Clayton Vic 3800, Australia
[27] Xi'an Jiaotong–Liverpool University, department of Mathematical Sciences, 111 Ren?ai road, Suzhou Dushu Lake Higher Education town,Jiangsu Province, China, cp 215123
[28] NOVA Optical Infrared Instrumentation Group, Oude Hoogeveensedijk 4, 7991 PD Dwingeloo, The Netherlands